

Temperature dependency of the optical properties of photovoltaic module component layers



Simon M.F. Zhang^{a,*}, Angus Gentle^a, Maryna Bilokur^{a,b}, Ning Song^a, Zhen Yang^a, Yajie Jiang^a, Hamish Teasdale^a, Raghavi Bhoopathy^a, Ivan Perez-Wurfl^a, Ziv Hameiri^a

^a School of Photovoltaic and Renewable Energy Engineering, University of New South Wales, Sydney, NSW, 2052, Australia

^b Research School of Physics, The Australian National University, Canberra, ACT, 2601, Australia

ABSTRACT

Photovoltaic module performance in the field is strongly dependent on the optical properties of its component layers and the temperature dependencies of these properties. However, despite their importance, the temperature dependencies of the optical properties of many photovoltaic module components appear to have not been characterised. Hence, the assumptions regarding their optical stabilities at various temperatures have not been verified. In this study, a temperature-dependent spectrophotometry method is developed to enable this verification. The temperature dependencies of the optical properties of silicon nitride, ethylene vinyl acetate (EVA), and backsheets are characterised, and their impacts on module operations are quantified via ray-tracing simulations. It is concluded that (1) silicon nitride anti-reflection coatings are optically stable between room temperature and 85 °C, and (2) several temperature dependencies exist at different wavelengths in both EVA and backsheets, however, they do not have a significant impact on the module operation.

1. Introduction

Photovoltaic (PV) modules generate power by converting light to electricity. Under typical field conditions of 1000 W/m², modern PV modules often operate at temperatures (T') of up to approximately 70 °C [1], while the temperature of older modules can reach 85 °C [2]. Therefore, to accurately predict their performance in the field, it is critical to study the temperature dependence of PV modules. This includes examining the temperature dependency of the optical properties of both the solar cells, where the energy conversion takes place, and other layers that are integrated into commercial modules which significantly impact the illumination received by the solar cells. However, existing studies of PV temperature dependence generally focus on the temperature coefficients (TC) of the solar cells [3,4], with very few investigations into the optical temperature dependency of other module components [5,6]. Instead, an implicit assumption is often made that each layer performs the same across the operating temperature range of PV modules [4,7].

For certain materials such as glass and glass anti-reflection coating (ARC), such optical stability is documented [5,6]. Yet, for most PV module components, such as encapsulants like ethylene-vinyl acetate

(EVA) and backsheets [primary polyethylene terephthalate (PET)], similar evidence appears to be absent in existing literature. This absence of evidence is especially relevant since the refractive index (n) of EVA at 589 nm has been recorded to reduce with temperature [8], and PET possesses a glass transition temperature of approximately 75 °C [9]. Hence, changes in the optical properties of these layers in the temperature range of 65 °C–85 °C and in the spectral region of 300 nm to 2000 nm may be expected [1,2]. Even for silicon nitride (SiN_x) ARC, which has been extensively investigated, evidence regarding the temperature dependence of its optical properties seems to be missing. Therefore, it is crucial to verify the optical stability of each module component across the range of field temperatures and assess the impact of any optical temperature dependencies on the module performance.

For each material, several room temperature optical studies have been conducted. The method typically employed for SiN_x characterisation is spectroscopic ellipsometry. Early studies by Doshi et al. [10] and Jellison et al. [11] investigated the room temperature optical properties of a wide range of SiN_x stoichiometries over a spectral range of 250 nm–840 nm. Later studies, such as that by Vogt [12], extended the spectral range to 250–1700 nm and obtained n and extinction coefficient (k) of SiN_x . For EVA, almost all optical characterisations have been

* Corresponding author.

E-mail address: mengfei.zhang@unswalumni.com (S.M.F. Zhang).

¹ To avoid confusion regarding abbreviations, in this study, transmittance is referred to as "T%" (and reflectance "R%"), and temperature is referred to as "T" (T-prime). "R&T" refers to reflectance and transmittance measurements, while "R&T(T)" refers to the temperature-dependent version of the same. In the body of this paper, "room temperature" and "high temperature" are always written in full, whereas they are sometimes in abbreviated as "RT" and "HT" in the figures.

Table 1

SiN_x samples target optical parameters, fabrication conditions, and measurement parameters.

Sample	Target thickness [nm]	Target n_{630}	Pressure [mbar]	Deposition temperature [$^{\circ}\text{C}$]	NH ₃ :SiH ₄ flow ratio	Belt speed [cm/min]	SE system	SE temperature [$^{\circ}\text{C}$]
SiN _x -S	75	2.0	0.30	289	1.25	N/A	V-VASE	25, 88
SiN _x -D1	120	1.9	0.25	400	7.01	45	V-VASE	22, 85
SiN _x -D2	110	2.07	0.27	400	5.25	55	V-VASE	22, 85
SiN _x -D3	120	2.15	0.17	400	2.25	58	V-VASE	22, 84
SiN _x -D4	110	2.3	0.30	375	2.33	47	M-2000 DI	25, 100
SiN _x -D5	110	2.4	0.25	400	1.55	57	M-2000 DI	25, 100

performed using spectroscopic reflectance and transmittance (R&T), from which R% and T%, and thus n and k, can be obtained. Whereas earlier studies investigated glass/EVA/glass stacks [13,14], and were open to complications introduced by an additional material in the optical path, later efforts eliminated this uncertainty by focusing on standalone EVA layers [15,16]. Backsheets are also most commonly measured with R&T, as its key optical attribute is reflectance back into the module. Vogt [12] measured R% by itself at room temperature, whereas McIntosh et al. [17] and Geretschlager et al. [18] also measured T%.

In the present study, these room-temperature measurements for SiN_x ARC, EVA, and backsheets are extended to cover a wide temperature range, encompassing the entire field operation range of PV modules. We first develop a temperature-dependent version of the R&T measurements [R&T(T')]. We then investigate the assumptions regarding the optical stability of SiN_x, EVA, and backsheets; the first through temperature-dependent ellipsometry, and the latter two through the newly developed R&T(T') system. For all three material groups, we obtain estimates of the change in their optical properties between room temperature and a high temperature (above 65 °C). Then, the observed changes are used as inputs for a ray-tracing simulation to estimate their impact on module performance in the field.

2. Methodology

2.1. Samples and characterisation

2.1.1. Silicon nitride

The SiN_x ARCs used in PV modules are typically deposited using plasma-enhanced chemical vapour deposition (PECVD) systems [19], which can be classified as static or dynamic [20,21]. The latter is an inline process commonly used in industrial manufacturing due to its higher throughput and reduced need for manual handling [22]. However, the constant movement of the substrates with respect to the gas sources creates a complex optical depth profile [20].

In this study, six SiN_x layers were characterised. They were deposited on single-side-polished silicon (Si) wafers. SiN_x-S was deposited using a static system (AK800 from Roth&Rau [23]), while the SiN_x-D samples were deposited using a dynamic system (MAiA from Meyer Burger [24]). Table 1 summarises the target optical properties, fabrication conditions, and measurement parameters of these samples. The target n at 630 nm (n_{630}) of the investigated samples were evenly distributed from 1.9 to 2.4, encompassing the possible optimal refractive indices of solar cell ARCs [25].

The SiN_x samples were characterised using temperature-dependent spectroscopic ellipsometry [SE(T')], where the ellipsometric Ψ and Δ – representing the change in polarisation (amplitude and phase) as a light beam is reflected from a sample – were collected at room and high temperatures (above 80 °C), at the incident angles of 65°, 70°, and 75°. As reflected in Table 1, due to varying equipment availability, the SE(T') measurements were conducted using two ellipsometers. SiN_x-S, SiN_x-D1, SiN_x-D2, and SiN_x-D3 were measured using a V-VASE (J.A. Woollam), while SiN_x-D4 and SiN_x-D5 were measured using an M-2000 DI (J.A.

Woollam) ellipsometer. The V-VASE system measures in the spectral range of 300 nm to 2500 nm and features a temperature stage capable of open-air heating to 85 °C. The M-2000 DI, on the other hand, was used to collect data within the spectral range of 300 nm to 1687.5 nm with a custom sample holder that could achieve temperatures of more than 100 °C.

The collected ellipsometry data was analysed by fitting it to optical models using J.A. Woollam's WVASE software [26], aiming to determine the n and k at different temperatures. Typically, the SiN_x layer is simulated using a Tauc-Lorentz oscillator [27,28], and the entire stack is modelled following an air/roughness/SiN_x/Si structure ("Standard Model"). Within this framework, the parameters subject to fitting include the thicknesses of the SiN_x and roughness layers, the four Tauc-Lorentz variables: amplitude (A), Lorentz resonant energy (E_n), broadening factor (C), and bandgap (E_g), as well as $\epsilon_1(\infty)$, a constant offset in the determination of the real part of the dielectric function.

In this study, this Standard Model was used to fit the statically deposited SiN_x-S samples. However, the optically intricate SiN_x-D samples were fitted using the "Advanced Model" developed by Borojevic et al. [29,30]. This model has been proven to be highly suitable for dynamically deposited layers [29–31]. Employing graded Tauc-Lorentz parameters, the model accommodates the challenges associated with the aforementioned varied optical depth profile. Further details about the fitting procedure are given in Appendix A.

2.1.2. EVA

Historically, EVA has been the predominant PV encapsulant, having separated itself from alternatives by its excellent cost-to-performance ratio [32]. It accounts for ~70 % of the encapsulant market today [33]. In the past, ultraviolet light (UV) absorbers have typically been incorporated into EVA, forming UV-absorbing EVA [15]. In recent years, however, UV-transparent EVAs have increasingly been used, especially on top of the solar cell, with a resulting increase of ~1 % in the short-circuit current density (J_{sc}) [15,34].

In this study, a UV-transparent EVA from an industrial partner was investigated. The main sample examined was a standalone "bare EVA" sample, prepared by laminating an EVA sheet placed between two sheets of smooth polymer films (perfluoroalkoxyalkane, 3D Printers Online). After lamination (3S Modultec, S1815), these films were peeled off, resulting in a freestanding laminated EVA layer [35]. A supplemental glass/EVA/glass "sandwich" sample was also prepared using two microscope slides (Sail Brand, 7101). To ensure the thickness of the sandwiched EVA, a two-layer EVA film stack was used. Further fabrication details can be found in Appendix B.

R&T(T') measurements of the bare EVA sample were conducted using a spectrophotometer with a spectral range of 250 nm to 2000 nm (PerkinElmer, Lambda 1050). The same spectrophotometer was used for the glass sandwich sample, for which only R%(T') measurements were performed. Sample thicknesses were measured with a thickness gauge (Mitutoyo). The EVA sample details, along with their measurement temperatures, are summarised in Table 2. Table 2 shows an uncertainty of the bare EVA thickness of 0.10 mm (see Appendix B for its origins). Here a "central" version of the bare EVA featuring a thickness of 0.45

Table 2
EVA samples and R&T(T') measurement parameter.

Sample	EVA Thickness [mm]	R%(T') Temperature [$^{\circ}$ C]	T%(T') Temperature [$^{\circ}$ C]
Bare EVA	0.45 ± 0.10	23, 64	23, 64
Glass/EVA/glass	0.60 ± 0.03	23, 70	NA

mm is analysed, while the 0.35 mm and 0.55 mm “extreme” versions are discussed in Appendix G. Nevertheless, each thickness leads to identical conclusions.

The R&T(T') data obtained from the EVA sample was first filtered against outliers using a moving window method based on the variance [36] and derivative sign change [37] of the data window, as described in Appendix A. Next, the R&T(T') data was fitted in WVASE to extract the temperature-dependent n and k . EVA was modelled as a standalone substrate, using a Cauchy optical layer as the baseline and adding Gaussian and Lorentz oscillators to simulate local absorption bands [38]. Further details about this analysis procedure can be found in Appendix A.

2.1.3. Backsheets

There is a diverse range of commercial solar cell backsheets; a detailed review is given in Ref. [32]. Nearly all backsheets consist of three layers, with the centre layer being PET. For the outer layers, either

fluoropolymer films (F-film) or fluorine coatings (F-coating) are commonly employed, as fluorine provides good UV resistance which PET lacks. Common F-films include polyvinyl fluoride (PVF) and polyvinylidene fluoride (PVDF). Due to the commercial names of PVF (Tedlar) and PVDF (Kynar), backsheets with these materials on either side are often referred to as TPT and KPK, respectively.

In this study, five backsheet samples supplied by industrial and research partners were investigated, consisting of four types: one F-coating/PET/F-coating (CPC), one bare PET sheet, two PVDF/PET/F-coating (KPC) sheets from different manufacturers, and one KPK sheet. The R&T(T') measurements of these backsheets were conducted using the same spectrophotometer and in the same spectral range (250 nm–2000 nm) as the EVA samples. Their thicknesses were measured with the same thickness gauge. The backsheets samples and measurement details are summarised in Table 3.

2.2. Temperature-dependent spectrophotometry system

Spectrophotometry is based on the principle that the reflectance, transmittance, and absorptance of a beam of light through a sample sum to unity:

$$R\% + T\% + A\% = 100\% \quad 1$$

where A% is absorptance. Typically, R% and T% are separately measured, and A% is calculated using Equation (1).

Table 3
Backsheet samples and R&T(T') measurement parameters.

Sample	Structure (cell/middle/air)	Thickness [mm]	Source	R%(T') Temperature [$^{\circ}$ C]	T%(T') Temperature [$^{\circ}$ C]
CPC	F-coating/PET/F-coating	0.31 ± 0.01	Company A	23, 75	23, 75
KPC-1	F-coating/PET/PVDF	0.31 ± 0.01	Company A	23, 75	23, 75
KPC-2	F-coating/PET/PVDF	0.30 ± 0.01	Company B	23, 77	23, 77
KPK	PVDF/PET/PVDF	0.31 ± 0.01	Company A	23, 75	23, 75
PET	PET	0.28 ± 0.01	Institute A	23, 70	23, 70

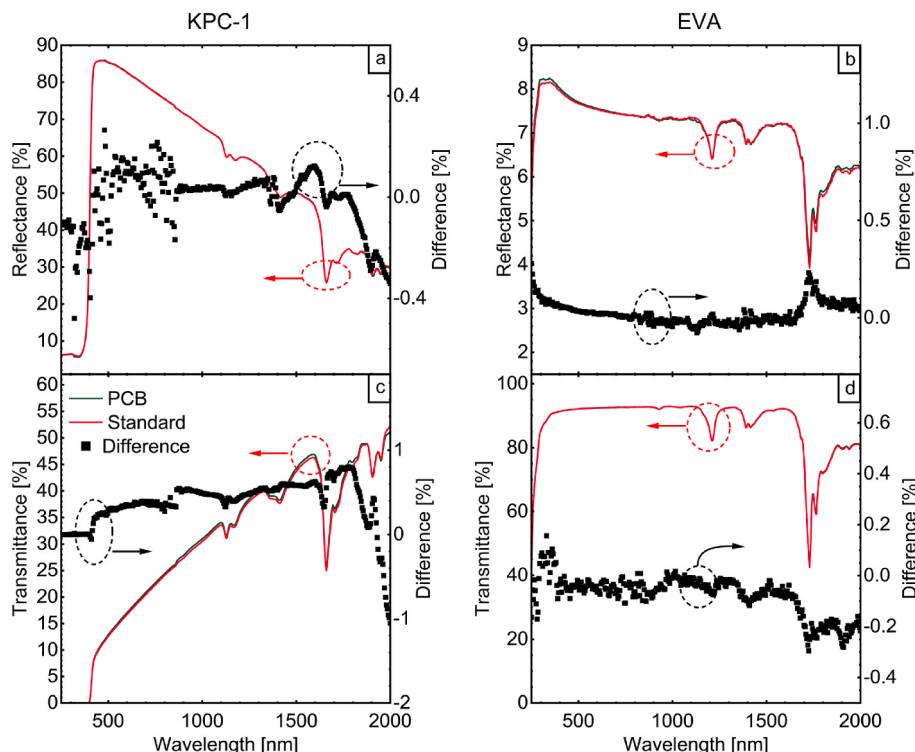


Fig. 1. Comparison between Standard and PCB-integrated measurements at room temperature. (a) R% for KPC-1, (b) R% for EVA, (c) T% for KPC-1, and (d) T% for EVA.

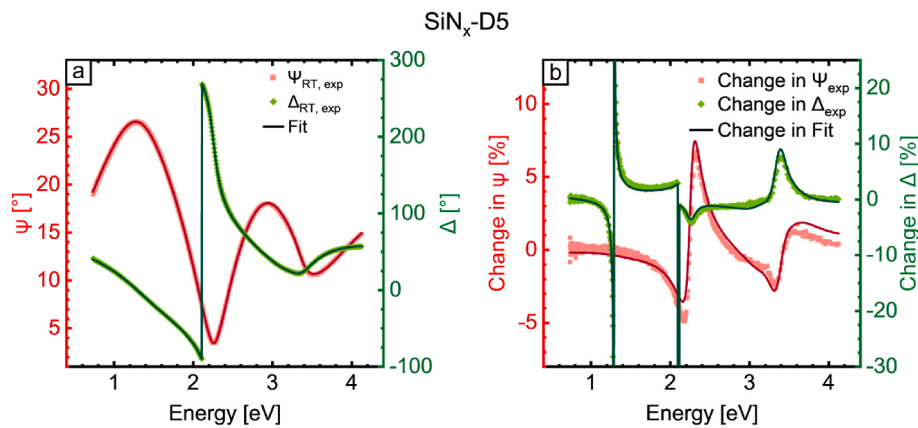


Fig. 2. The SE(T) experimental (exp) and fitted data for SiN_x-D5: (a) Ψ and Δ at an incident angle of 75° at room temperature (RT), and (b) the relative change in Ψ and Δ between room and high temperatures.

In this study, R&T(T') measurements were realised by combining a Lambda 1050 (PerkinElmer) spectrophotometer, a 150 mm integrating sphere accessory, and a resistive coil heater that was implemented on a printed circuit board (PCB). The samples were mounted onto the PCB and heated by passing a current through the coil. A circular aperture 15 mm in diameter in the centre of the PCB allows the beam to pass through to the sample and the integrating sphere. The sample temperature was monitored using a handheld infrared (IR) thermal imaging camera (FLIR), which consistently achieves a difference below 1 °C when compared to temperatures measured by K-type thermocouples. More information regarding this system is given in Appendix C.

Fig. 1 compares room temperature measurements conducted with the “Standard” R&T (without the PCB) and the R&T(T') (with the PCB) setups for both a highly transmitting EVA-T sample that is a sister sample of the main sample introduced in Section 2.1 and a highly reflective sample (backsheet KPC-1). As can be seen, the spectra with and without (Standard) the PCB agree well within 1 % (Fig. 1). Therefore, it seems the integration of the PCB has only a negligible impact on the accuracy of the measurement.

2.3. Ray-tracing simulations using SunSolve

For each of the three investigated sample types (SiN_x, EVA, and backsheets), ray-tracing simulations were performed to estimate the impact of the temperature-dependent changes of its optical properties on module performance. This simulation was performed using SunSolve [39], a web-based ray-tracing program widely used for a large variety of PV device simulations [40], including for Si solar cells and modules [41, 42], as well as perovskite and tandem modules [43]. Details of these simulations are given in Appendix D.

Table 4

Major fitting parameters of each of the SiN_x samples, together with the associated MSE. The uncertainties for each parameter are the 90 % confidence intervals reported by WVASE.

Sample and Temperature [°C]	SiN _x Thickness [nm]	Roughness Thickness [nm]	A [eV]	E _n [eV]	C [eV]	E _g [eV]	c ₁ (∞)	MSE	
SiN _x -S	25	72.22 ± 0.03	16.0 ± 0.1	64.4 ± 0.8	10.9 ± 0.1	7.3 ± 0.2	2.79 ± 0.01	1	4.6
	88			63.3 ± 0.8	10.8 ± 0.1	6.8 ± 0.2	2.79 ± 0.01		
SiN _x -D1	22	117.0 ± 0.4	5.3 ± 0.4	69.6 ± 1.4	9.3 ± 0.2	2.2 ± 0.1	Graded	0.91 ± 0.1	4.0
	85			70.1 ± 1.4	9.3 ± 0.2	2.3 ± 0.1		0.90 ± 0.1	
SiN _x -D2	22	108.6 ± 4.3	0.9 ± 4.9	Graded	9.0 ± 0.1	2.5 ± 0.1	2.57 ± 0.01	1	4.1
	85				9.0 ± 0.1	2.6 ± 0.1	2.57 ± 0.01		
SiN _x -D3	22	120.8 ± 0.1	3.5 ± 0.1	Graded	8.97 ± 0.05	4.6 ± 0.1	2.50 ± 0.01	1	3.6
	84				8.93 ± 0.05	4.6 ± 0.1	2.48 ± 0.01		
SiN _x -D4	25	112.7 ± 0.2	8.6 ± 0.1	Graded	5.70 ± 0.04	5.9 ± 0.1	Graded	1.75 ± 0.04	5.7
	100				5.63 ± 0.04	6.0 ± 0.1		1.64 ± 0.04	
SiN _x -D5	25	104.1 ± 0.4	6.9 ± 0.4	Graded	4.76 ± 0.04	6.0 ± 0.2	Graded	1.38 ± 0.04	5.5
	100				4.65 ± 0.04	5.9 ± 0.2		1.50 ± 0.04	

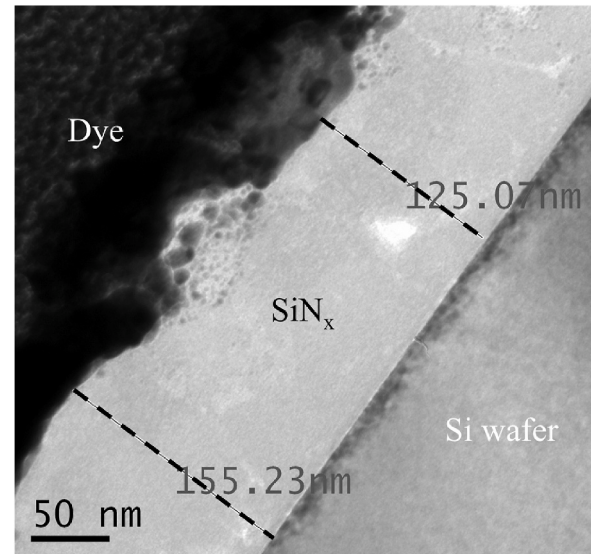


Fig. 3. A cross-sectional TEM image of a sister sample to SiN_x-S.

3. Results and discussion

3.1. Silicon nitride

Fig. 2(a) shows the measured and fitted Ψ and Δ of a representative sample (SiN_x-D5) at room temperature, showcasing an excellent fit. Fig. 2(b) presents the percentage change in Ψ and Δ between room and

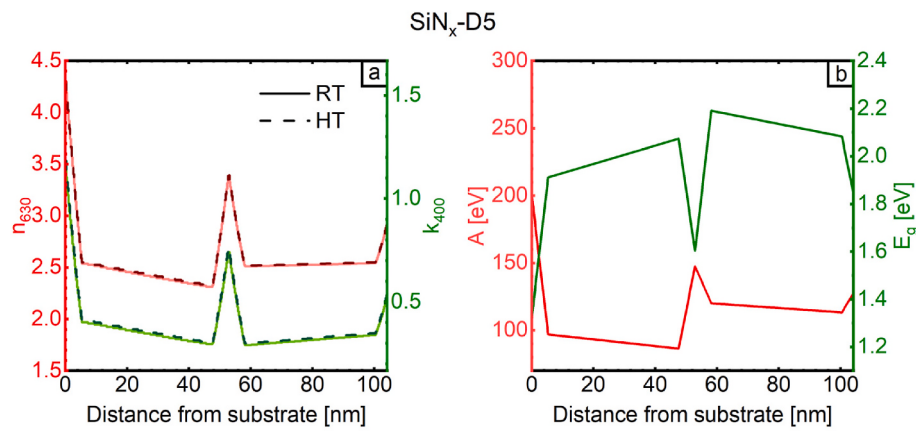


Fig. 4. The optical depth profile of SiN_x -D5: (a) n_{630} and k_{400} , and (b) the Tauc-Lorentz parameters A and E_g .

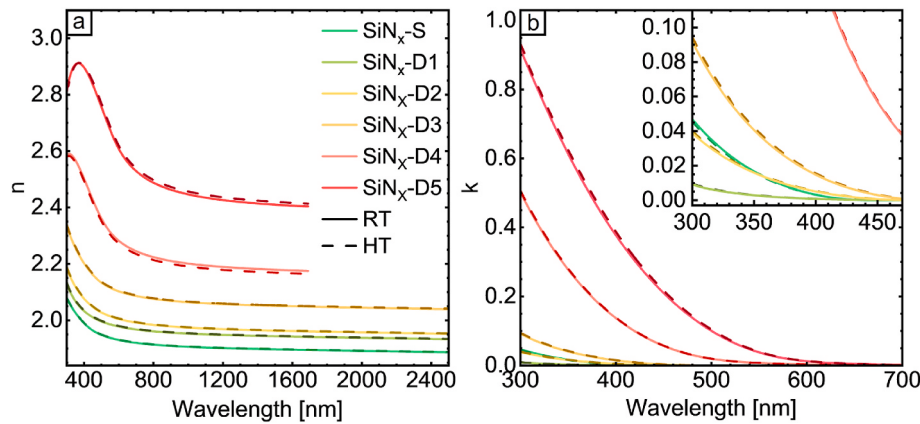


Fig. 5. Comparisons between the room and high temperature (RT and HT) optical properties of all the SiN_x samples: (a) n , and (b) k , with the inset showing the expanded view of the 300 nm–470 nm spectral region.

high temperatures. The excellent match between the changes in the experimental and the modelled data further showcases the high quality of the fits achieved. The magnitude of these differences is almost entirely below 10 %. This small temperature dependency is also reflected in the fitting parameters (as shown in Table 4); the parameter changes are generally smaller than 1 %, falling within the 90 % confidence interval reported by WVASE, regarded here as the uncertainty range. Similar results were obtained for all the other samples as summarised in Table 4 and Appendix E. The excellent fit quality is evident from the low mean squared error (MSE) observed across all samples.

One interesting feature revealed in Table 4 is the larger-than-expected thickness of the surface roughness of the SiN_x -S sample (16 ± 0.1 nm). Typically, the surface roughness of SiN_x does not exceed a few nanometres [11]. To confirm the existence of this unusually thick

roughness and validate the plausibility of the fit, a transmission electron microscopy (TEM) measurement was conducted on a sister sample with a target SiN_x thickness of 150 nm and correspondingly an even thicker fitted surface roughness. The TEM image is shown in Fig. 3, revealing a SiN_x thickness variation of approximately 30 nm. As surface roughness serves as an effective medium approximation of the mixture of the otherwise topmost layer and air, such a wide variation of film thickness substantiates the high thickness of the roughness layer in these samples. This high surface roughness may be caused by the relatively low total gas flow rate during the deposition of SiN_x -S (270 sccm) [44]. Confirming the presence of this unexpected feature, discovered during the fitting process, further underscores the precision of the employed fitting methodology.

As illustrated in Fig. 4, the Advanced Model produces depth profiles of both n and k [Fig. 4 (a)] at each wavelength by employing graded fitting parameters [Fig. 4(b)]. These depth profiles align with the anticipated behaviour of dynamically deposited samples [29,30]. Fig. 4 (a) also compares the n_{630} and k_{400} depth profiles of SiN_x -D5 at room and high temperatures and shows that they are almost identical. Similar observations were made for the depth profiles of other samples, as seen in Appendix F.

Following the methodology outlined in Ref. [30], the effective n and k dispersions of the samples fitted with the Advanced Model were obtained using a weighted average of the n and k depth profiles at each wavelength. The n and k dispersions of all the investigated SiN_x samples are presented for both room and high temperatures in Fig. 5. As intended, the six investigated samples encompass a wide range of optical parameters, with n_{630} values ranging from 1.93 to 2.54. Fig. 5 further

Table 5

The determined J_{sc} (at room temperature) of simulated PV modules that use the extracted n and k of the investigated SiN_x samples, and the differences in J_{sc} and parasitic absorption (J_{para}) between room and high temperatures. The uncertainties are 95 % confidence intervals reported by SunSolve. All current densities are relative to the module area.

Sample	n_{630}	J_{sc} [mA/cm^2]	ΔJ_{sc} [mA/cm^2]	ΔJ_{para} [mA/cm^2]
SiN_x -S	1.93	37.54 ± 0.05	-0.01 ± 0.09	-0.002 ± 0.126
SiN_x -D1	1.98	37.59 ± 0.05	-0.01 ± 0.09	-0.01 ± 0.15
SiN_x -D2	2.00	37.57 ± 0.05	-0.02 ± 0.10	0.01 ± 0.13
SiN_x -D3	2.10	37.47 ± 0.05	-0.01 ± 0.10	0.03 ± 0.13
SiN_x -D4	2.26	36.32 ± 0.05	-0.05 ± 0.09	0.01 ± 0.16
SiN_x -D5	2.55	34.59 ± 0.04	-0.12 ± 0.09	0.07 ± 0.17

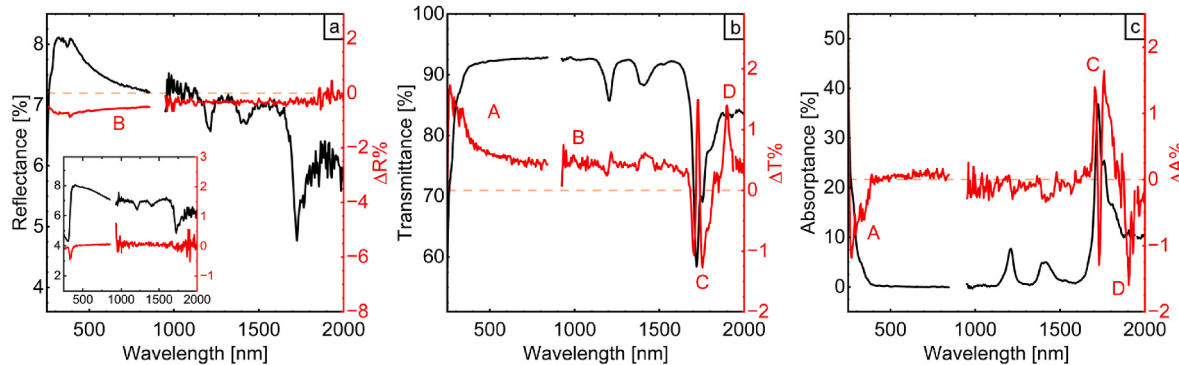


Fig. 6. R&T(T') of the bare EVA sample. (a) Room temperature R% and change in R% between room and high temperatures ($\Delta R\%$), (b) T% and $\Delta T\%$, and (c) A% and $\Delta A\%$. The inset to (a) shows the R%(T') measurement of the glass sandwich sample.

shows that changes in both n and k are small, on the order of approximately 0.01 in magnitude.

Table 5 summarises the results of ray tracing simulations for each sample at room and high temperatures. At room temperature, for SiN_x ARCs with n_{630} between ~ 1.93 and ~ 2.10 , the J_{sc} of the simulated module (see Appendix D for details) displays only small variations within uncertainty. However, for n_{630} above 2.25, J_{sc} reduces by more than 3 %. This is consistent with previous reports indicating that the optimal n_{630} for SiN_x ARC for Si cells is approximately two [25,45,46]. The table also summarises the changes in J_{sc} and parasitic absorption between the room and high temperature measurements. For the former, all changes are within 0.05 mA/cm² and much smaller than the uncertainty reported by SunSolve (except for SiN_x -D5, which is within 35 % of the uncertainty range) and constitute a maximum of 0.14 % of J_{sc} magnitude, not typically considered significant in field operation. As this level of change is expected to occur at around 100 °C, for the large majority of field operations, the module J_{sc} is expected to be influenced by only a fraction of this small amount. This is consistent with temperature-dependent quantum efficiency measurements of Si cells featuring SiN_x ARCs [3,47], which reveal that the temperature dependence of J_{sc} is almost completely due to the band gap narrowing effects of the Si wafer, and thus unrelated to SiN_x . Changes in cell-and-module parasitic absorption are similarly small, and should not significantly influence module field operation through, for example, changing its operation temperature. Hence, on the levels of measured data, fitted parameters, and simulated performance impacts, there is no significant temperature dependency in the optical properties of SiN_x ARC.

3.2. EVA

After data filtering according to the procedure outlined in Appendix

A, the R&T(T') measurements of the main EVA sample are presented in Fig. 6, where A% is calculated according to Equation (1). The spectra presented in black show the R&T measurements at room temperature. These measurements resemble that of a typical UV-transparent EVA film, with an 80 % UV-cutoff of ~ 290 nm [48], a maximum T% of above 93 % between ~ 400 nm and 1150 nm, and various absorption peaks at 1210 nm and above [49,50]. The red lines in Fig. 6 show the difference between the R%, T%, and A% at room and high temperatures. The four largest differences are labelled Features A to D.

Feature A is a reduction in A% at high temperature below ~ 385 nm and a corresponding increase in T%. This is probably due to a contraction in the bandgap of EVA with increasing temperature [51].

Feature B can be seen in Fig. 6(a) and (b) as a broadband reduction in R% and an increase in T% of around 0.5 % at high temperature. As no corresponding A% change is seen in Fig. 6(c), this implies that Feature B does not include an absorption component, and is instead caused by a temperature-dependent reduction in the n of EVA between (at least) 250 nm and 2000 nm, which lowers R% and raises T%. This conclusion is supported by the R%(T') measurements conducted on the same EVA material encapsulated in a glass sandwich, as shown in the inset of Fig. 6(a). As the EVA n is extremely similar to that of glass, a small change in the n of the former does not significantly affect the optical coupling between the two layers, contributing only negligibly to a change in the R % of the sandwich. Since glass is optically stable [6] in this temperature range, Fig. 6(a)'s inset shows that Feature B in the glass/EVA/glass stack is approximately zero.

Feature C is a series of three peaks and valleys in the $\Delta T\%$ and $\Delta A\%$ spectra near 1750 nm, corresponding to two A% peaks at room temperature, likely due to the first overtone of the carbon-hydrogen (C-H) bond's stretching mode [50,52]. At high temperatures, the A% peak at 1725 nm seems to blueshift by ~ 1 nm, and the peak at 1760 nm

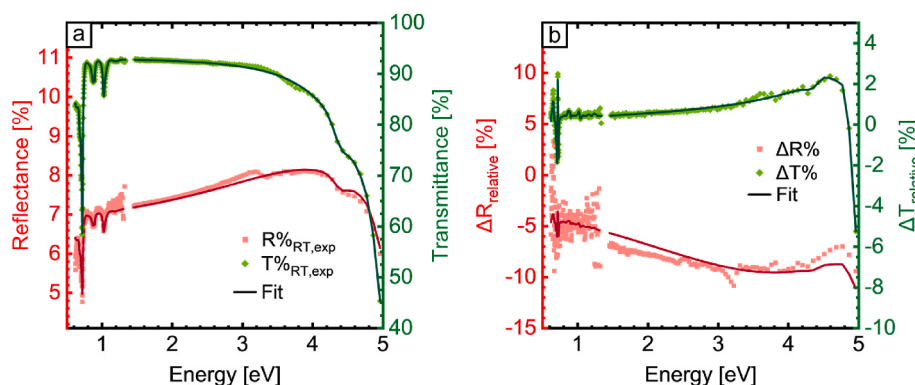


Fig. 7. R&T(T') experimental (exp) and fitted data for the bare EVA sample: (a) R&T at room temperature (RT), (b) the relative change in R&T% between room and high temperatures.

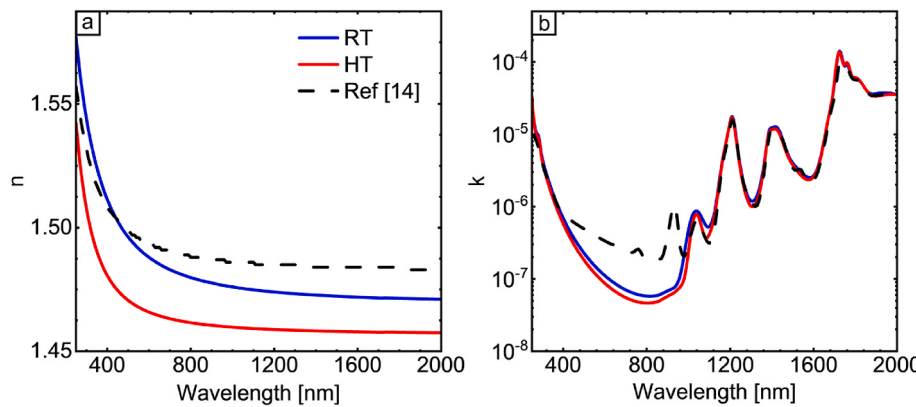


Fig. 8. The room and high temperature (RT and HT) optical properties of the investigated EVA sample, with a UV-transparent EVA [15] for comparison: (a) n, and (b) k.

increases in magnitude, resulting in the three peaks and valleys seen in Fig. 6(b) and (c).

Feature D is a reduction in A% at high temperatures between ~ 1875 nm and 2000 nm and a corresponding increase in the high-temperature T% in the same range. This is likely due to the large number of absorption bands in this spectral range [52], stemming from complex combination modes of C-H and C-O (oxygen) bonds.

Fig. 7(a) presents an excellent agreement between the measured and fitted R&T at room temperature, while Fig. 7(b) shows a good agreement between the experimental and fitted relative changes in the R&T between the room and high temperature measurements. The measured and fitted R&T(T') of the 0.35 mm and 0.55 mm thick EVAs present similar quality, and are shown in Appendix G. The fitted WVASE parameters of these samples are also detailed in the same appendix, where MSEs of 0.13 reflect the excellent qualities of the fits.

The temperature-dependent n and k of the bare EVA sample were extracted from the fit shown in Fig. 7 and presented in Fig. 8, along with that of a UV-transparent EVA from Ref. [15]. At room temperature, the optical properties of the presently investigated EVA sample are extremely similar to that of the sample of Ref [15]. This similarity includes the n (within 0.02), and most of the examined spectrum for the k. Between ~ 400 nm and ~ 850 nm, the k of the investigated EVA is more than 50 % lower than the sample of Ref [15], showing improvement over the encapsulant studied in 2016. Between ~ 850 nm and ~ 950 nm, a significant number of data points were removed due to being outliers (see Appendix A). Consequently, the small peak shown by Ref [15] sample centred around 940 nm is not present in the investigated EVA.

Compared to room temperature, at 64 °C, the investigated EVA sample shows a reduction in n throughout the examined spectrum (by a median of 0.02 from 300 nm to 1200 nm), but k appears to reduce only minimally (median 5×10^{-8} in the same range). This validates the earlier inference that Feature B in Fig. 6 is caused by a change in n. Appendix G shows the same patterns of change for fits performed with thicknesses of 0.35 mm and 0.55 mm.

The reduction in n is consistent with the Lorentz-Lorenz equation [53], which states that the temperature-dependent change in n of a material is proportional to the negative of its thermal expansion coefficient. As EVA expands with increasing temperature [54,55], its density of polarisable molecules decrease, resulting in a reduction in n. At 590 nm, n reduces by ~ 0.023 , consistent with the ~ 0.029 predicted at 589 nm in Ref. [8].

The temperature-dependent n and k of Fig. 8 were substituted into SunSolve to model their impact on module operation, with the results shown in Table 6. For the examined EVA sample, the n and k changes over ~ 40 °C induce a negligible ΔJ_{sc} and a ΔJ_{para} of ~ -0.15 mA/cm 2 . As the last column of Table 6 shows, there is a lack of correlation between ΔJ_{sc} and ΔJ_{para} , likely due to an increase in light escaping from the front

Table 6

SunSolve simulation results: the temperature-dependent impact of EVA optics on module performance. All current densities are relative to the module area.

Temperature	J_{sc} [mA/cm 2]	J_{para} [mA/cm 2]	$J_{esc, front}$ [mA/cm 2]
23 °C	37.54 ± 0.04	11.84 ± 0.06	10.32 ± 0.04
64 °C	37.53 ± 0.04	11.69 ± 0.07	10.46 ± 0.04

module surface ($\Delta J_{esc, front}$). This, in turn, is likely caused by an increase in the reflection at the front glass/EVA interface due to the reduced n coupling [56] between the two layers at the higher temperature. Notably, this change of only ~ 0.2 % of the 61.3 mA/cm 2 incident illumination is consistent with the negligible $\Delta R\%$ observed in the inset of Fig. 6(a).

As parasitic absorption has no direct impact on the electrical performance of the module, this appears to indicate that the waste heat generated by the module reduces by ~ 0.15 mA/cm 2 near 64 °C as compared to 23 °C. To evaluate this effect in Watts, the product of the AM1.5G illumination intensity and the absorptance of each module layer was integrated over the spectral range of 300 nm to 2000 nm (see Appendix H for details). It was found that the 0.15 mA/cm 2 reduction in parasitic absorption equates to a power loss reduction of approximately 2 W/m 2 . This represents only ~ 0.3 % of all losses in the module, a seemingly negligible amount. By balancing power absorption, radiation, and convection using Equation (A1) (see Appendix H for details), the difference in the module temperature when using the EVA parameters at 64 °C as opposed to 23 °C was estimated to be 0.1 °C. This small difference is negligible for field operation and is highly likely to be dominated by other effects, such as dust accumulation. This further confirms that the optical changes in the EVA layers do not have a significant impact on PV module operation in the field.

3.3. Backsheets

The room temperature R&T measurements of the backsheets samples are presented in Fig. 9, where A% is calculated according to Equation (1).

Firstly, it can be seen that all backsheets exhibit similar spectral shapes in all three aspects. Of these, the R% shape has been reported previously [17,18]. Below approximately 1000 nm, the CPC and KPK samples display marginally lower (~ 5 %) R% than the other samples. In the case of CPC, this correlates with its increased T% in the same range. KPK, however, shows a further reduced T% throughout the measured spectral range, likely due to its higher A%, attributed to its use of double PVDF layers.

For all samples, the significant dips in R&T occur at similar wavelengths and can be attributed to peaks in A%. Since these peaks exist in

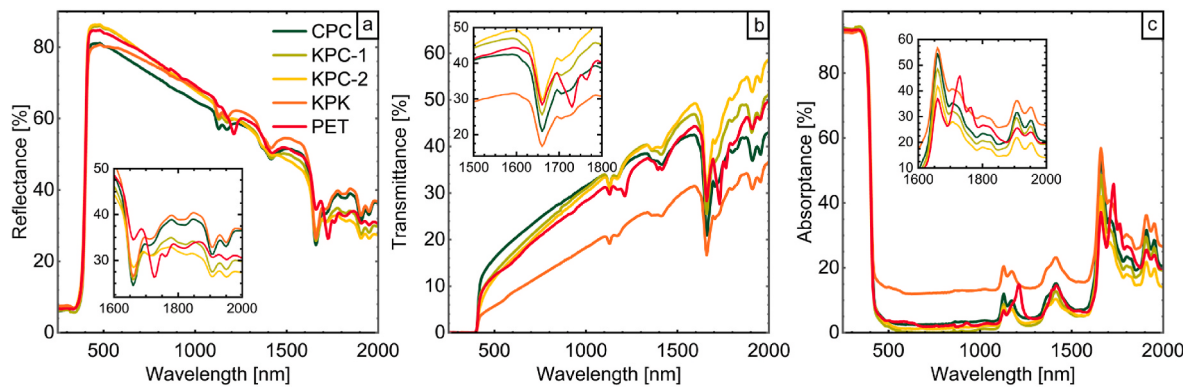


Fig. 9. Room temperature R&T measurements of the investigated backsheets: (a) R%, with the inset showing the expanded view between 1600 nm and 2000 nm; (b) T%, with the inset showing the expanded view between 1500 nm and 1800 nm; and (c) A%, with the inset showing the expanded view between 1600 nm and 2000 nm.

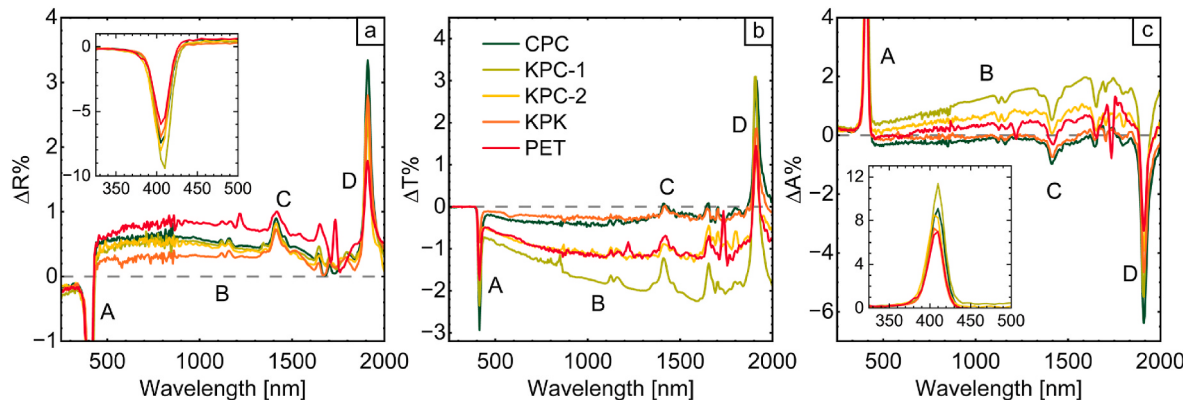


Fig. 10. Differences between the room and high temperature R&T measurements. (a) $\Delta R\%$ of all five backsheet samples, with the inset showing the full view between 325 nm and 500 nm, (b) $\Delta T\%$, and (c) $\Delta A\%$, with the inset showing the full view between 325 nm and 500 nm.

all the investigated backsheets, it appears they originate from the central PET layer. Among these, the major peak near 1660 nm likely reflects the first overtone of the C-H stretching mode in aromatic compounds [57]. Two additional peaks can be seen in the bare PET sample near 1215 nm and 1730 nm; these likely represent the first and second overtones of the C-H aliphatic stretching mode [52,57].

The difference between R%, T%, and A% at room and high temperatures is shown in Fig. 10. The four largest features labelled A to D are shared across all samples.

Feature A, depicted as a sharp increase in A% between approximately 360 nm and 430 nm, arises from the shift in A% edge peak to higher wavelengths with heating as seen in Fig. 10. Since this feature is evident across all samples, it signifies a modification in the bandgap of the underlying PET layer. Figs. 9 and 10 indicate that this bandgap is approximately 400 nm (3.1 eV). Given that previously reported PET bandgaps are around 4 eV [58,59], it is likely that the observed bandgap is not attributed to the PET polymer backbone but rather to the UV absorbers added to enhance the backsheet stability. One potential UV absorber that might have caused this cutoff is titanium oxide (TiO_2), which features a bandgap range of ~ 2.1 eV– ~ 3.2 eV, depending on the doping material [60].

Feature B is the broadband increase in R% and A% as well as the reduction in T% between approximately 460 nm and 1900 nm. It seems to affect each sample to different degrees, changing the R% of all samples but appearing close to zero for the CPC and KPK samples in T% and A%. Nevertheless, as the feature with the largest area under the curve below ~ 1200 nm, it is the primary candidate for any impact on the module performance. This impact is evaluated in the next subsection.

Features C and D are R% and T% increases and A% reductions at approximately 1415 nm and 1910 nm, respectively. They correspond to dips in R% and T% and peaks in A% at the same wavelengths at room temperature in Fig. 9. These wavelengths match well with the absorption bands found for oxygen-hydrogen (O-H) bonds in water sorbed in PET [61,62]. As the temperature increases, more water molecules located on the surface or interior of the backsheet evaporate, reducing the A% observed at these wavelengths. As PV module laminations are performed at temperatures above 100 °C and the encapsulant layers have the function of preventing moisture ingress during the module's lifetime [63], it is not expected that Features C or D have a significant impact on module operation.

To evaluate the impact of these temperature-dependent changes on module operation, PET and KPC-1, the samples showing the largest $\Delta R\%$ and $\Delta T\%$, respectively, were selected for module impact evaluation. As backsheets in PV modules are attached to encapsulants, the R&T used to evaluate its impact on module performance must be that of the encapsulated backsheets, which differ significantly from those measured in the air [12,17]. In this study, the results of the R&T(T') measurements conducted in the air were converted to that of the encapsulated variants using the backsheet optical calculator developed by McIntosh et al. [17,64]. This tool assumes that the backsheet can be modelled as an ideal pigmented reflector and that the optical properties of the material that surrounds this pigment are the same as those of the encapsulant material located above the backsheet. To maximise the effect of the optical changes in the backsheet on module operation, a UV-transmitting EVA [15] was selected to be the binder and encapsulant material.

The in-air and encapsulated R%, T%, and A% for KPC-1 are shown in

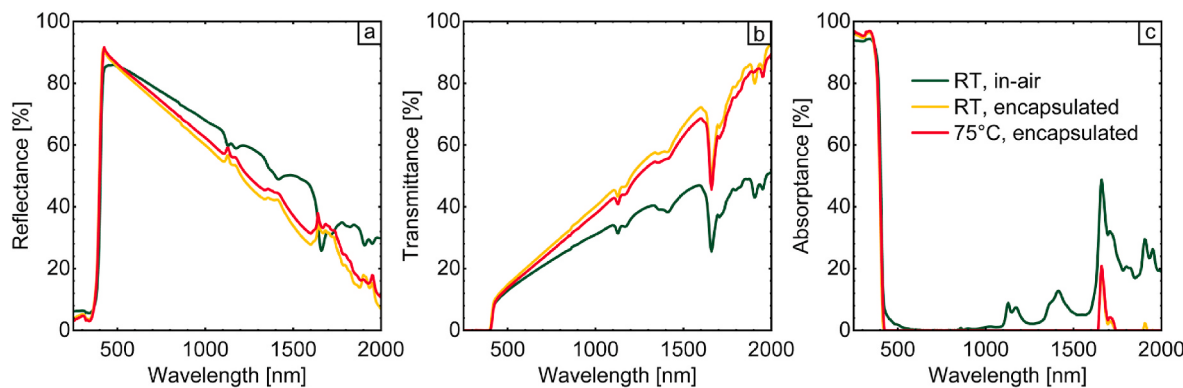


Fig. 11. The optical properties of the KPC-1 backsheets as measured in air at room temperature, and as calculated after encapsulation at room temperature and 75 °C: (a) R%, (b) T%, and (c) A%.

Table 7

SunSolve simulation results: the temperature-dependent impact of backsheets on module performance. All current densities are relative to the module area.

Sample	Temperature	J_{sc} [mA/cm^2]	J_{para} [mA/cm^2]
KPC-1	23 °C	37.14 ± 0.04	8.48 ± 0.06
	75 °C	37.15 ± 0.04	8.54 ± 0.06
PET	23 °C	37.18 ± 0.04	8.48 ± 0.06
	70 °C	37.17 ± 0.04	8.54 ± 0.06

Fig. 11. Comparing them, the biggest difference is the large increase in T % and therefore reduction in A%. This is in agreement with previous observations [64]. Between room temperature and 75 °C, the R% of KPC-1 shows a ~1 % increase, and T% shows a similarly sized reduction, like the in-air measurements. These trends are also displayed by the PET sample.

Substituting these encapsulated R&T(T') measurements into the SunSolve model, the impact on module operation is reported in Table 7. As can be seen, the changes in backsheets optical properties have no detectable impact on J_{sc} .

This is supported by previous records of identical J_{sc} temperature dependencies between the monofacial and bifacial versions of the same module [65,66], implying that the backsheets has no impact. Changes in the optical properties of the backsheets also cause a J_{para} increase of approximately 0.06 mA/cm^2 for both backsheets samples. However, this change is not only smaller than the uncertainty range but also opposite in direction and smaller than the <2 % ΔJ_{para} observed for EVA. Therefore, its impact on module operation is expected to be negligible.

4. Conclusions

This study investigated the temperature dependency in the optical parameters of PV module component layers, including SiN_x ARCs, EVA, and backsheets.

For SiN_x ARCs, no detectable temperature dependence in optical properties were found. Hence, it was concluded that they can be considered optically stable over the range of operational temperatures for PV modules. To enable temperature-dependent optical characterisation of EVA and backsheets, an R&T(T') system was developed and presented. Using this system, several small temperature dependencies were found in the optical properties of both EVA and backsheets. However, through ray-tracing simulations, the effects of these dependencies on module operation were ultimately found to be negligible. Thus, the implicit assumptions of the optical stability of SiN_x , EVA, and backsheets appear to be justified.

This study focused on common Si module components due to the current predominance of Si technologies. However, the techniques

developed and demonstrated in this study are versatile and can easily be transferred to study other materials, including those popularly used with other solar cell materials and architectures such as perovskites, chalcogenides, and tandem solar cells.

CRediT authorship contribution statement

Simon M.F. Zhang: Writing – review & editing, Writing – original draft, Visualization, Validation, Project administration, Methodology, Investigation, Formal analysis, Data curation. **Angus Gentle:** Writing – review & editing, Validation, Resources, Methodology, Investigation, Formal analysis. **Maryna Bilokur:** Writing – review & editing, Resources, Methodology, Investigation. **Ning Song:** Writing – review & editing, Resources, Methodology. **Zhen Yang:** Writing – review & editing, Methodology, Investigation. **Yajie Jiang:** Resources, Methodology. **Hamish Teasdale:** Methodology, Investigation. **Raghavi Bhopathi:** Supervision, Resources, Methodology. **Ivan Perez-Wurfl:** Writing – review & editing, Validation, Supervision, Resources, Methodology, Investigation, Formal analysis. **Ziv Hameiri:** Writing – review & editing, Writing – original draft, Validation, Supervision, Resources, Project administration, Methodology, Funding acquisition, Formal analysis, Conceptualization.

Declaration of competing interest

The authors declare that they have no known competing financial interests or personal relationships that could have appeared to influence the work reported in this paper.

Acknowledgement

The authors want to thank Zubair Abdullah-Vetter (UNSW) for providing samples, and Keith McIntosh (PV Lighthouse) and Gernot Oreski (Polymer Competence Center Leoben) for valuable discussions. This work was supported by the Australian Government through the Australian Renewable Energy Agency [ARENA; project 2022/TRAC001]. The views expressed herein are not necessarily the views of the Australian Government, and the Australian Government does not accept responsibility for any information or advice contained herein. Simon M. F. Zhang was supported by an Australian Government Research Training Program Scholarship.

Appendix A. Supplementary data

Supplementary data to this article can be found online at <https://doi.org/10.1016/j.solmat.2024.113389>.

Data availability

Data will be made available on request.

References

- [1] I. Santiago, D. Trillo-Montero, I.M. Moreno-Garcia, V. Pallarés-López, J.J. Luna-Rodríguez, Modeling of photovoltaic cell temperature losses: a review and a practice case in South Spain, *Renew. Sustain. Energy Rev.* 90 (2018) 70–89.
- [2] J.A. Duffie, W.A. Beckman, *Solar Engineering of Thermal Processes*, third ed., Wiley, Hoboken, New Jersey, 2006.
- [3] S.M.F. Zhang, et al., Illumination-dependent temperature coefficients of the electrical parameters of modern silicon solar cell architectures, *Nano Energy* 98 (2022) 107221.
- [4] J. Haschke, et al., The impact of silicon solar cell architecture and cell interconnection on energy yield in hot and sunny climates, *Energy Environ. Sci.* 10 (5) (2017) 1196–1206.
- [5] J. Gong, R. Dai, Z. Wang, C. Zhang, X. Yuan, Z. Zhang, Temperature dependent optical constants for SiO_2 film on Si substrate by ellipsometry, *Mater. Res. Express* 4 (8) (2017) 085005.
- [6] G. Ghosh, Sellmeier coefficients and dispersion of thermo-optic coefficients for some optical glasses, *Appl. Opt.* 36 (7) (1997) 1540.
- [7] M. Piliouigne, A. Oukaja, M. Sidrach-de-Cardona, G. Spagnuolo, Temperature coefficients of degraded crystalline silicon photovoltaic modules at outdoor conditions, *Prog. Photovoltaics Res. Appl.* 29 (5) (2021) 558–570.
- [8] U. Bernini, P. Russo, M. Malinconico, E. Martucelli, M.G. Volpeau, P. Mormile, Temperature dependent optical properties of a synthesis blend of poly(methyl methacrylate) and vinyl rubber, *J. Mater. Sci.* 28 (23) (1993) 6399–6402.
- [9] J. Zhou, et al., Temperature-dependent breakdown and pre-breakdown conduction of polyethylene terephthalate, *J. Phys. D Appl. Phys.* 55 (36) (2022).
- [10] P. Doshi, G.E. Jellison, A. Rohatgi, Characterization and optimization of absorbing plasma-enhanced chemical vapor deposited antireflection coatings for silicon photovoltaics, *Appl. Opt.* 36 (30) (1997) 7826.
- [11] G.E. Jellison, F.A. Modine, P. Doshi, A. Rohatgi, Spectroscopic ellipsometry characterization of thin-film silicon nitride, *Thin Solid Films* 313–314 (1–2) (1998) 193–197.
- [12] M.R. Vogt, Development of physical models for the simulation of optical properties of solar modules, der Gottfried Wilhelm Leibniz Universität (2015).
- [13] K.R. McIntosh, N.E. Powell, A.W. Norris, J.N. Cotsell, B.M. Ketola, The effect of damp-heat and UV aging tests on the optical properties of silicone and EVA encapsulants, *Prog. Photovoltaics Res. Appl.* 19 (2011) 294–300.
- [14] H. Nagel, A.G. Aberle, R. Hezel, Optimised antireflection coatings for planar silicon solar cells using remote PECVD silicon nitride and porous silicon dioxide, *Prog. Photovoltaics Res. Appl.* 7 (1999) 245–260.
- [15] M.R. Vogt, et al., Optical constants of UV transparent EVA and the impact on the PV module output power under realistic irradiation, *Energy Proc.* 92 (2016) 523–530.
- [16] J. Eymard, R. Clerc, V. Duveiller, B. Commault, M. Hebert, Characterization of UV–Vis–NIR optical constants of encapsulant for accurate determination of absorption and backscattering losses in photovoltaic modules, *Sol. Energy Mater. Sol. Cells* 240 (2022) 111717.
- [17] K.R. McIntosh, J. Jung, M.D. Abbott, B.A. Sudbury, Determination and evaluation of a backsheet's intrinsic reflectance, *AIP Conf. Proc.* 1999 (2018).
- [18] K.J. Geretschläger, G.M. Wallner, J. Fischer, Structure and basic properties of photovoltaic module backsheet films, *Sol. Energy Mater. Sol. Cells* 144 (2016) 451–456.
- [19] Z. Hameiri, Laser-Doped Selective Emitter and Local Back Surface Field Solar Cells with Rear Passivation, University of New South Wales, 2010.
- [20] S. Winderbaum, et al., Unveiling the differences between dynamic and static deposition of PECVD silicon nitride for solar cells, in: 20th European Photovoltaic Solar Energy Conference, 2005, pp. 1301–1304.
- [21] Armin G. Aberle, Overview on SiN surface passivation of crystalline silicon solar cells, *Sol. Energy Mater. Sol. Cells* 65 (2001) 239–248.
- [22] H.P. Sperlich, D. Decker, P. Saint-Cast, E. Erben, L. Peters, High productive solar cell passivation on Roth&Rau MAIA® MW-PECVD inline machine – a comparison of Al_2O_3 , SiO_2 and $\text{SiN}_x\text{-H}$ process conditions and performance, in: 5th World Conference on Photovoltaic Energy Conversion, 2010, pp. 1352–1357.
- [23] A.G. Roth & Rau, Operating manual: AK 800 - RIE/PECVD system, Roth & Rau AG, Hohenstein-Ernstthal (2007).
- [24] D. Sontag, et al., The MAIA 2.1 Platform from Roth & Rau – The Latest Generation of a Highly Flexible Coating System for the PV Industry, Roth & Rau AG, Hohenstein-Ernstthal, 2014.
- [25] A. El Amrani, et al., Determination of the suitable refractive index of solar cells silicon nitride, Superlattice. *Microst.* 73 (2014) 224–231.
- [26] J.A. Woollam Co, Guide to Using WVASE Spectroscopic Ellipsometry Data Acquisition and Analysis Software, Nebraska, Lincoln, 2012.
- [27] G.E. Jellison, F.A. Modine, Parameterization of the optical functions of amorphous materials in the interband region, *Appl. Phys. Lett.* 69 (3) (1996) 371–373.
- [28] G.E. Jellison, F.A. Modine, Erratum: 'Parameterization of the optical functions of amorphous materials in the interband region, *Appl. Phys. Lett.* 69 (14) (1996) 2137.
- [29] N. Borojevic, Z. Hameiri, S. Winderbaum, Advanced optical modelling of dynamically deposited silicon nitride layers, *Appl. Phys. Lett.* 109 (2) (2016), 021903–021903.
- [30] N. Borojevic, Z. Hameiri, S. Winderbaum, Advanced optical characterisation of industrial PECVD silicon nitride layers, in: 32nd European Photovoltaic Solar Energy Conference, 2016.
- [31] Z. Hameiri, N. Borojevic, L. Mai, N. Nandakumar, K. Kim, S. Winderbaum, Low-absorbing and thermally stable industrial silicon nitride films with very low surface recombination, *IEEE J. Photovoltaics* 7 (4) (2017) 996–1003.
- [32] S.K. Chunduri, M. Schmela, Market Survey - Backsheets and Encapsulation 2022–2023, 2023.
- [33] ITRPV, International technology roadmap for photovoltaic (ITRPV) - 2022 results [Online]. Available: <https://www.vdma.org/international-technology-roadmap-photovoltaic>, 2023.
- [34] A. Sinha, K. Hurst, S. Ulicna, L.T. Schelhas, D.C. Miller, P. Hacke, Assessing UV-induced degradation in bifacial modules of different cell technologies, in: 48th IEEE Photovoltaic Specialists Conference, 2021, pp. 767–770.
- [35] B.M. Chen, C.Y. Peng, J.L. Cho, G.A. Porter, Optimization of solar module encapsulant lamination by optical constant determination of ethylene-vinyl acetate, *Int. J. Photoenergy* 2015 (2015) 276404.
- [36] S. Xu, M. Baldea, T.F. Edgar, W. Wojsznis, T. Blevins, M. Nixon, An improved methodology for outlier detection in dynamic datasets, *AIChE J.* 61 (2) (Feb. 2015) 419–433.
- [37] A. Zhang, S. Song, J. Wang, Sequential data cleaning: a statistical approach, in: ACM SIGMOD International Conference on Management of Data, 2016, pp. 909–924.
- [38] B. Hajduk, H. Bednarski, B. Trzebicka, Temperature-dependent spectroscopic ellipsometry of thin polymer films, *J. Phys. Chem. B* 124 (16) (2020) 3229–3251.
- [39] PV Lighthouse, SunSolve. <https://www.pvlighthouse.com.au/sunsolve>. (Accessed 20 October 2018).
- [40] PV Lighthouse, SunSolve publications. <https://sunsolve.info/publications/>. (Accessed 3 December 2024).
- [41] R. Preu, E. Lohmüller, S. Lohmüller, P. Saint-Cast, J.M. Greulich, Passivated emitter and rear cell - devices, technology, and modeling, *Appl. Phys. Rev.* 7 (2020) 041315.
- [42] I. Haedrich, D.C. Jordan, M. Ernst, Methodology to predict annual yield losses and gains caused by solar module design and materials under field exposure, *Sol. Energy Mater. Sol. Cells* 202 (2019) 110069.
- [43] L. Xu, et al., Parasitic heating of perovskite- and silicon-based photovoltaics, *Adv. Energy Mater.* 13 (2023) 1–11.
- [44] M.C. Wei, S.J. Chang, C.Y. Tsia, C.H. Liu, S.C. Chen, SiN_x deposited by in-line PECVD for multi-crystalline silicon solar cells, *Sol. Energy* 80 (2) (2006) 215–219.
- [45] J.F. Lelièvre, E. Fourmond, A. Kaminski, O. Palais, D. Balltaud, M. Lemiti, Study of the composition of hydrogenated silicon nitride $\text{SiN}_x\text{-H}$ for efficient surface and bulk passivation of silicon, *Sol. Energy Mater. Sol. Cells* 93 (8) (2009) 1281–1289.
- [46] J.F. Lelièvre, A. Kaminska, J.P. Boyeaug, R. Monnab, M. Lemiti, Optical properties of PECVD and UVCVD $\text{SiN}_x\text{-H}$ antireflection coatings for silicon solar cells, in: 31st IEEE Photovoltaic Specialists Conference, 2005, pp. 1111–1114.
- [47] Y. Hishikawa, et al., Temperature dependence of the short circuit current and spectral responsivity of various kinds of crystalline silicon photovoltaic devices, *Jpn. J. Appl. Phys.* 57 (2018) 18RG17.
- [48] Hangzhou First Applied Material, Firstpvpm product page. https://www.firstpvpm.com/en/pro_profile.asp?cid=203&aid=159#auto. (Accessed 4 May 2024).
- [49] J. Morse, M. Thuis, D. Holsapple, R. Willis, M.D. Kempe, D.C. Miller, Degradation in photovoltaic encapsulant transmittance: results of the second PVQAT TG5 artificial weathering study, *Prog. Photovoltaics Res. Appl.* 30 (7) (2022) 763–783.
- [50] T. Furukawa, et al., On-line monitoring of melt-extrusion transesterification of ethylene vinylacetate copolymers by near infrared spectroscopy and chemometrics, *J. Near Infrared Spectrosc.* 10 (3) (2002) 195–202.
- [51] H.G. Harish Kumar, R.D. Mathad, K.S.S. Sarma, G. Sanjeev, C.R. Haramagatti, Electron-beam irradiation effects on poly(ethylene-co-vinyl acetate) polymer, *Radiat. Eff. Defect Solid* 166 (3) (2011) 198–207.
- [52] J. Workman Jr., L. Weyer, Practical Guide and Spectral Atlas for Interpretive Near-Infrared Spectroscopy, second ed., CRC Press, Boca Raton, 2012.
- [53] S. Takahashi, H. Okada, S. Nobukawa, M. Yamaguchi, Optical properties of polymer blends composed of poly(methyl methacrylate) and ethylene-vinyl acetate copolymer, *Eur. Polym. J.* 48 (2012) 974–980.
- [54] Netsch, EVA: ethylene vinyl acetate. <https://analyzing-testing.netzsch.com/en/polymers-netzsch-com/commodity-thermoplastics/eva-ethylene-vinyl-acetate>. (Accessed 5 May 2024).
- [55] P. Romer, K.B. Pethani, A.J. Beinert, Effect of inhomogeneous loads on the mechanics of PV modules, *Prog. Photovoltaics Res. Appl.* 32 (2024) 84–101.
- [56] M.R. Vogt, et al., Measurement of the optical constants of soda-lime glasses in dependence of iron content and modeling of iron-related power losses in crystalline si solar cell modules, *IEEE J. Photovoltaics* 6 (2016) 111–118.
- [57] H. Lammers, M.P.B. Van Uum, J.P. De Kleijn, Process analysis: properties of poly(ethylene terephthalate) measured by near infrared spectroscopy, 2a. In-line analysis of poly(ethylene terephthalate) melt, *Macromol. Chem. Phys.* 196 (6) (1995) 2029–2034.
- [58] S. Aarya Siddhartha, K. Dev, S.K. Raghuvaran, J.B.M. Krishna, M.A. Wahab, Effect of gamma radiation on the structural and optical properties of Polyethyleneterephthalate (PET) polymer, *Radiat. Phys. Chem.* 81 (4) (2012) 458–462.
- [59] K. Chikaoui, M. Izzerouen, M. Djebara, M. Abdesselam, Polyethylene terephthalate degradation under reactor neutron irradiation, *Radiat. Phys. Chem.* 130 (2017) 431–435.
- [60] R.V. Nair, V.S. Gummaluri, M.V. Matham, C. Vijayan, A review on optical bandgap engineering in TiO_2 nanostructures via doping and intrinsic vacancy modulation towards visible light applications, *J. Phys. D Appl. Phys.* 55 (31) (2022).

- [61] G. Lachenal, Characterization of poly(ethylene terephthalate) using near and far FTIR spectroscopy, *Int. J. Polym. Anal. Char.* 3 (2) (1997) 145–158.
- [62] M. Fukuda, H. Kawai, N. Yagi, O. Kimura, T. Ohta, FTi.r. study on the nature of water sorbed in poly(ethylene terephthalate) film, *Polymer* 31 (2) (1990) 295–302.
- [63] M.C.C. de Oliveira, A.S.A. Diniz Cardoso, M.M. Viana, V. de F.C. Lins, The causes and effects of degradation of encapsulant ethylene vinyl acetate copolymer (EVA) in crystalline silicon photovoltaic modules: a review, *Renew. Sustain. Energy Rev.* 81 (2018) 2299–2317.
- [64] PV Lighthouse, The optical properties of an encapsulated backsheet. <https://www.pvlighthouse.com.au/cms/lectures/white-papers/optical/bsr-encaps-vs-unencaps>, 2022. (Accessed 17 August 2023).
- [65] JinkoSolar, “Product Specifications: Tiger Pro 72HC-TV Bifacial.”.
- [66] JinkoSolar, “Product Specifications: Tiger Pro 72HC.”.